RESEARCH ARTICLE

Improving the Capacity of NOMA Network Using Multiple Aerial Intelligent Reflecting Surfaces

LE SI PHU[1], TAN N. NGUYEN[1], (Member, IEEE), MIROSLAV VOZNAK[1], (Senior Member, IEEE), BA CAO NGUYEN[2], TRAN MANH HOANG[2], BUI VU MINH[3], AND PHUONG T. TRAN[4], (Senior Member, IEEE)

[1]Faculty of Electrical Engineering and Computer Science, VSB—Technical University of Ostrava, 70800 Ostrava, Czech Republic
[2]Faculty of Basic Techniques, Telecommunications University, Nha Trang, Khanh Hoa 650000, Vietnam
[3]Faculty of Mechanical, Electrical, Electronic and Automotive Engineering, Nguyen Tat Thanh University, Ho Chi Minh City 754000, Vietnam
[4]Wireless Communications Research Group, Faculty of Electrical and Electronics Engineering, Ton Duc Thang University, Ho Chi Minh City 70000, Vietnam

Corresponding author: Phuong T. Tran (tranthanhphuong@tdtu.edu.vn)

ABSTRACT In this paper, we propose to utilize multiple aerial intelligent reflecting surfaces (AIRSs) for significantly enhancing the ergodic capacity of a non-orthogonal multiple access (NOMA) network. Unlike previous works where only one AIRS was often utilized to support only two NOMA users, Q AIRSs and L users are applied in the proposed NOMA-AIRS network. We mathematically derive the ergodic capacity (EC) expressions at the multiple users of the proposed NOMA-AIRS network over Nakagami-m channels recommended for use in the fifth and beyond generations (5G & B5G) of mobile communications. Numerical results show that the proposed NOMA-AIRS network can deeply exploit the advantages of AIRSs. In particular, by using $Q = 4$ AIRSs where each AIRS has 20 reflecting elements (REs), the ECs of the proposed NOMA-AIRS network are significantly higher than the ECs of the conventional NOMA network (without AIRSs). Moreover, the ECs of the proposed NOMA-AIRS network can be two times higher than those of the conventional NOMA network in the low transmit power regime. However, if the transmit power is high enough, the benefits of AIRSs are reduced due to the NOMA features. Besides confirming the advantages of AIRSs, the effects of key parameters such as the number of REs and total of REs in the AIRSs, bandwidth, altitudes of AIRSs, and carrier frequency are thoroughly determined. Based on the achieved observations, we give some recommendations to enhance the EC performance of the proposed NOMA-AIRS network in practice scenarios.

INDEX TERMS Non-orthogonal multiple access, aerial intelligent reflecting surface, multiuser systems, moment functions, ergodic capacity.

I. INTRODUCTION

Recently, intelligent reflecting surface (IRS) has emerged as an effective solution to dramatically enhance the performance and coverage of future wireless networks [1], [2]. In particular, IRS can intelligently reflect the radio frequency (RF) signals without signal processing and power supply

The associate editor coordinating the review of this manuscript and approving it for publication was Eyuphan Bulut.

[3], [4]. Compared with conventional relays, the IRS has many benefits even with small size. More specifically, the outage probability and the symbol error rate of the IRS-aided wireless systems are dramatically lower than those of the conventional amplify-and-forward relay-aided wireless systems [5]. Meanwhile, the ergodic capacity (EC) of the IRS-aided wireless systems is greatly higher than the EC of the conventional decode-and-forward relay-aided wireless systems [6]. Moreover, the spectral efficiency of using IRS is

also higher than that of using relays because IRS can operate in full-duplex transmission [3]. As the results, utilizing IRS can achieve higher performance and higher power and spectral efficiencies in comparison with the conventional relays [3], [5], [6], [7]. Therefore, IRS becomes an effective technical solution to deploy in the beyond-fifth-generation (B5G) of wireless systems [8], [9], [10].

Besides the ground IRS, a groundbreaking advancement in wireless communication technology is the aerial IRS (AIRS) [11], [12]. Unlike ground IRS, which is typically deployed as passive surfaces fixed to buildings or walls, the AIRS takes innovation to new heights by incorporating drone-based technology. These flying platforms are equipped with intelligent reflecting elements (REs) that can dynamically adjust their orientation and positions in real-time, allowing for unparalleled flexibility and adaptability in manipulating wireless signals [11], [12], [13]. By strategically positioning itself in the vicinity of communication nodes or users, the AIRS optimizes signal propagation, enhances coverage, and mitigates signal blockages in a highly efficient manner [14]. This transformative technology holds immense potential in various applications, including disaster recovery, remote sensing, and emergency communications, where traditional infrastructure may be limited or unavailable [11], [12], [13], [15]. Consequently, the AIRS can support to open a new era of agile and responsive wireless networks deployed in the B5G systems [12], [16].

In order to exploit the advantages of IRS, it is combined with other new technologies such as full-duplex, unmanned aerial vehicle, and nonorthogonal multiple access (NOMA) [16], [17], [18], [19], [20], [21], [22]. Particularly, NOMA technologies are revolutionary paradigms in wireless systems. Unlike traditional orthogonal multiple access technologies, NOMA offers an innovative approach that enables multiple users to simultaneously access the same resources in a non-orthogonal manner, thereby significantly improving spectral efficiency and accommodating a larger number of users within a given communication channel [19]. As a result, when IRS is combined with NOMA, the performance and coverage as well as the number of users of wireless systems are dramatically enhanced [16], [18], [19], [23], [24]. However, a combination of AIRS and NOMA was not studied. In the meanwhile, exploiting both AIRS and NOMA technologies will bring many benefits to wireless systems deployed in the fifth generation (5G) and B5G networks.

In the recent reports, AIRS was utilized to aid wireless systems [11], [12], [13], [14], [25], [26]. In particular, an AIRS operating as a relay was deployed to forward signals from a transmitter to a receiver. Specifically, the outage probability, cumulative density function, and ergodic capacity (EC) are often derived to investigate the behaviors of the AIRS-aided wireless systems [11], [12], [14], [25], [27], [28]. Moreover, the cases of imperfect channel state information (CSI) and successive interference cancellation at NOMA users were also determined [29]. Their results confirmed

that using AIRS can provide better performance than using relay. It is because the line-of-sight (LoS) components can be available between the transmitter/receiver and AIRS due to the high altitudes of AIRS. Meanwhile, it is difficult to achieve these components with conventional relay because of blocking objects [14]. However, only one AIRS was often used to aid communications between one transmitter/source and one receiver/user. There is a lack of studies regarding the mathematical analysis in the case that multiple AIRSs aided multiuser systems adopting NOMA schemes.

As aforementioned, the usage of either IRS or multiple IRSs to aid NOMA networks has been widely studied. However, several works were using an AIRS to aid single-user networks. Meanwhile, multiple AIRSs and multiple users are more suitable in practice due to the high capacity requirements of 5G & B5G networks. More specifically, the weights of AIRSs are often limited, it isn't easy to utilize one big-size AIRS in practice. Moreover, the operation time of AIRSs is also limited, thus, when one AIRS cannot aid the transmitter-user communications, the other AIRSs can still reflect the RF signals between the transmitter and users. Therefore, the received signal power at the users is reliable with multiple AIRSs. More specifically, multiple AIRSs can be found in various locations, while one AIRS is situated in only one specific location. Therefore, when using only one AIRS, users may not receive signals if there are obstructions in the transmission path from the transmitter to the AIRS or from the AIRS to the users [7]. In this context, having multiple AIRSs located in different places can address this problem. This is because, in cases where signals reflected by one or two AIRSs are unavailable to users due to obstructions, signals reflected by other AIRSs remain accessible to users. As a result, the received signal strength at the users is significantly boosted compared to the scenario involving just one AIRS. In other words, cooperative communications are utilized at multiple users to improve the reliability and the performance of wireless systems using multiple AIRSs. In addition, it is easy to have the LoS components between the transmitter/users and AIRSs due to the flexible movements of AIRSs. These issues motivate us to propose a wireless network where multiple AIRSs are utilized to aid multiple NOMA users. Besides multiple AIRSs and NOMA users, we also use the practical Nakagami-*m* channels recommended for 5G & B5G in the proposed NOMA-AIRS network. Consequently, the proposed NOMA-AIRS network and its behaviors are significantly different to the previous works. The main contributions of this paper are summarized as follows:

- We propose to use multiple AIRSs to support multiuser adopting NOMA schemes applied in 5G & B5G networks (shortened as the proposed NOMA-AIRS network). Importantly, we exploit both the advanced reflecting links introduced by AIRSs and the conventional transmitter-user links to improve the reliability and performance of the proposed network. In other words, the conventional links used in 5G and the

Notation	Description
$\Pr\{.\}$	Probability of an event
$\mathbb{E}\{.\}$	Expectation operator
$\mathcal{CN}(\mu, \sigma^2)$	Gaussian noise with mean μ and variance σ^2
$\Gamma(.)$	Gamma function
$\mathcal{K}_a(.)$	The a order modified Bessel function of the second kind
$F(.)$	Cumulative distribution function (CDF)
$\Gamma(.,.)$	Upper incomplete gamma function
$f(.)$	Probability density function (PDF)
$\exp(.)$	Exponential function
$\gamma(.,.)$	Lower incomplete gamma function
$G_{.,.}^{.,.}(.)$	Meijer function

advanced links used in B5G are combined in the proposed NOMA-AIRS network.

- We obtain the exact expressions of ECs at users of the proposed NOMA-AIRS network over practical Nakagami-m environments recommended to utilize in 5G & B5G standards.[1] It is obvious that the obtained expressions are more complex than those of the previous works where only one AIRS and only one user were used [11], [12], [14], [25]. We provide Monte-Carlo simulations to confirm the accuracy of the derived expressions.

- We confirm the advantages of the proposed NOMA-AIRS network by comparing its ECs with those of the conventional NOMA network (without AIRSs). Specifically, the ECs of the proposed NOMA-AIRS network are significantly higher than the ECs of the conventional NOMA network even with the total of REs being 80. In the low transmit power regime, the ECs of the proposed NOMA-AIRS network can be two times higher than those of the conventional NOMA network. However, when the transmit power is high enough, the benefits of AIRSs are reduced due to the NOMA features. Moreover, we determine the effects of key parameters such as the number of REs and total of REs in the AIRSs, bandwidth, altitudes of AIRSs, and carrier frequency on the ECs of the proposed network. Based on the achieved observations, some recommendations to enhance the EC performance of the proposed NOMA-AIRS network in practice scenarios are given.

The rest of this paper is organized as follows. The system and signal model of the proposed NOMA-AIRS network are detailedly presented in Section II. The mathematical derivations to obtain the EC expressions are provided in Section III. The numerical results are clarified in Section IV. Finally, the remarked conclusions are presented in Section V. For better

---

[1]Besides mathematical analysis, measurement experiment is another method often utilized [8], [9]. Although this method can reflect the realistic characteristics of the AIRS-aided wireless systems and it is easy to propose algorithms and solutions to improve the system performance, it took a lot of effort and time to obtain the research results. Meanwhile, mathematical analysis can provide rigorous analysis on the system performance and it is easy to obtain the system behaviors based on the derived expressions. However, it is difficult to propose algorithms or solutions to improve the system performance because of computational complexity in mathematical derivations.

readability, the mathematical notations are summarized in Tab. 1.

II. SYSTEM MODEL

Fig. 1 illustrates the block diagram of the proposed NOMA-AIRS network where a source (S) transmits messages to L users (D_1, D_2, ..., and D_L) under the aiding of Q AIRSs. To dramatically enhance the received signal power, the conventional S-user links and advanced S-AIRS-user links are combined at the users. In addition, S and L users are single antenna devices.[2] Meanwhile, the qth AIRS ($q = 1, 2, \ldots, Q$) includes K_q REs. Moreover, the distances between S and users satisfy the NOMA principles, e.g., $d_{SD_1} > d_{SD_2} > \ldots > d_{SD_L}$, where $d_{SD_1}, d_{SD_2}, \ldots, d_{SD_L}$ are the distances from S to $D_1, D_2, \ldots,$ and D_L, respectively. In other words, D_L is the nearest user while D_1 is the furthest user in the proposed NOMA-AIRS network.

From the NOMA principles, the transmitted message x_S of S is combined from L messages corresponding to L users. In particular, S uses the power-domain superposition coding to combine L messages. Therefore, x_S is expressed as $x_S = \sqrt{\rho_1 P_S} x_1 + \sqrt{\rho_2 P_S} x_2 + \ldots + \sqrt{\rho_L P_S} x_L = \sum_{l=1}^{L} \sqrt{\rho_l P_S} x_l$, where ρ_l and x_l are the power allocation coefficient and message for the lth user, respectively; $P_S = \mathbb{E}\{|x_S|^2\}$ is the average transmit power of S. Due to the distributions of $D_1, D_2, \ldots,$ and D_L, $\rho_1, \rho_2, \ldots,$ and ρ_L have to satisfy $\rho_1 > \rho_2 > \ldots > \rho_L$ and $\rho_1 + \rho_2 + \ldots + \rho_L = \sum_{l=1}^{L} \rho_l = 1$.[3]

At the tth user (D_t, $t = 1, 2, \ldots, L$), the received message is formulated as[4]

$$y_t = \Big(\sum_{q=1}^{Q} \sum_{k=1}^{K_q} h_{qk} g_{qk} e^{j\varphi_{qk}} + n_{st} \Big) \sum_{l=1}^{L} \sqrt{\rho_l P_S} x_l + z_t, \quad (1)$$

---

[2]This paper examines multiple AIRSs, resulting in a highly intricate received signal at users due to the abundance of reflected channels from these AIRSs. Consequently, mathematically analyzing the performance of the proposed NOMA-AIRS network with multiple antennas at S is a challenging task. The case of multiple AIRSs aid NOMA network with multi-antenna transmitter can be considered in our future works.

[3]It is noteworthy that the distribution of users is deterministic in the time duration of information transmission. In other words, the messages ($x_1, x_2, \ldots,$ and x_L) and power levels ($\rho_1, \rho_2, \ldots,$ and ρ_L) are predefined before S transmits messages [30]. Importantly, the users may be mobile and their positions change dynamically. In this circumstance, S will reallocate the power allocation coefficients and messages based on the NOMA user information. Meanwhile, the distribution of AIRSs can be either deterministic or stochastic, and the choice depends on the specific use case and deployment strategy. Deterministic distributions are common in planned network deployments, while stochastic distributions are more typical in dynamic or mobile environments where AIRS locations are subject to change.

[4]Besides utilizing all AIRSs for transmission, the best-selected AIRSs can be performed in the proposed NOMA-AIRS network. Specifically, both approaches were performed in the multi-IRS-aided wireless systems [7], [31]. It has been demonstrated that both approaches possess their own sets of advantages and drawbacks. Particularly, the first scheme (all AIRSs are utilized) may yield superior performance but comes at the cost of increased complexity and greater demands on the fronthaul/backhaul infrastructure. Conversely, in the second scheme (some AIRSs are selected), the remaining AIRSs can be allocated for alternative purposes, such as assisting other pairs of users [7]. In this paper, we opt for the first scheme due to its ability to deliver superior performance compared to the second scheme.
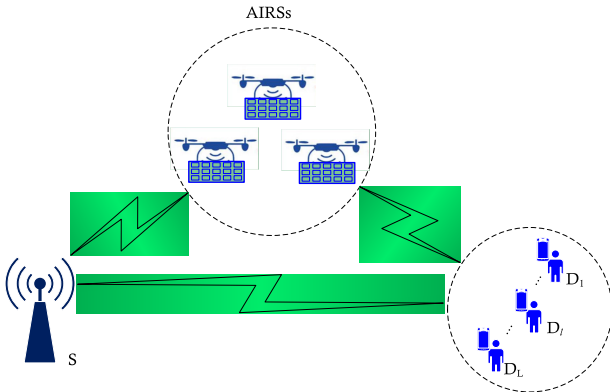
FIGURE 1. Illustration of the proposed NOMA-AIRS network.

where h_{qk}, g_{qk} and n_{st} are the channel gains from S to the kth RE of the qth AIRS (shortened as the $(k/q)^{th}$), from the $(k/q)^{th}$ to D_t,[5] and from S to D_t, respectively; φ_{qk} denotes the phase of the $(k/q)^{th}$; $z_t \sim \mathcal{CN}(0, \sigma_t^2)$ denotes the Gaussian noise at D_t. It is noteworthy that to derive the practical performance of the proposed NOMA-AIRS network, the Gaussian noise at D_t is calculated from bandwidth (B_w), noise figure (N_f), and thermal noise power density (N_0) [32], i.e.,

$$\sigma_t^2 = 10 \log(B_w) + N_f + N_0. \tag{2}$$

Since the channel gains are complex numbers, they can be represented via the magnitudes and phases, e.g., $h_{qk} = |h_{qk}|e^{-j\theta_{qk}}$, $g_{qk} = |g_{qk}|e^{-j\psi_{qk}}$ and $n_{st} = |n_{st}|e^{-j\phi_{st}}$ where $|h_{qk}|$, $|g_{qk}|$, and $|n_{st}|$ are the magnitudes and θ_{qk}, ψ_{qk}, and ϕ_{st} are the phases of h_{qk}, g_{qk} and n_{st}, respectively. Therefore, we can represent (1) as

$$y_t = \left(\sum_{q=1}^{Q} \sum_{k=1}^{K_q} |h_{qk}|e^{-j\theta_{qk}} e^{j\varphi_{qk}} |g_{qk}|e^{-j\psi_{qk}} + |n_{st}|e^{-j\phi_{st}} \right)$$
$$\times \sum_{l=1}^{L} \sqrt{\rho_l P_S} x_l + z_t. \tag{3}$$

Now, we organize (3) as

$$y_t = e^{-j\phi_{st}} \left(\sum_{q=1}^{Q} \sum_{k=1}^{K_q} |h_{qk}||g_{qk}|e^{j(\varphi_{qk} - \theta_{qk} - \psi_{qk} + \phi_{st})} + |n_{st}| \right)$$
$$\times \sum_{l=1}^{L} \sqrt{\rho_l P_S} x_l + z_t. \tag{4}$$

As confirmed in the literature, in the context of AIRS/IRS-aided communications utilizing training signals, two commonly employed methods for achieving accurate channel state information (CSI) are: one involving RF chains and the other without RF chains [33]. When RF chains are utilized, the estimation of S-AIRS/IRS and AIRS/IRS-user

channels can be performed independently at the AIRSs/IRSs. Conversely, in scenarios without RF chains, the estimation focuses on concatenated S-AIRS/IRS-user channels [33], [34]. Furthermore, given the rapid advancements in computing hardware and software, particularly the progress in deep learning and optimization algorithms, channel estimation for the proposed NOMA-AIRS network can be effectively implemented [34]. These methods allow to obtain perfect CSI in the proposed NOMA-AIRS network. It's worth noting that the assumption of perfect CSI has been widely adopted in prior research endeavors [9], [11], [12], [13], [14], [25].

As presented in the previous section, a big advantage of AIRSs/IRSs is their independently adjusted phases in the case of perfect CSI for greatly enhancing the received power [25], [31], [35]. In particular, the configuration of AIRS/IRS comprises two-dimensional meta-surface arrays under the control of at least one microcontroller. These arrays possess the capability to customize the manipulation of incoming electromagnetic fields [3], [5]. More specifically, each individual meta-surface can independently modify the phase shift (PS) of the electromagnetic waves, thereby allowing for coordinated efforts in creating an optimized wireless communication channel. Additionally, through the utilization of communication-oriented software, the PSs of the REs can be dynamically regulated. Consequently, real-time adjustments to the PSs enable precise control over the reflected waves [36]. Notably, the PSs of REs are dependent on the diodes employed in the AIRSs/IRSs [32], [37]. Due to hardware limitations, practical scenarios involve discrete rather than continuous PS adjustments, making discrete PSs more suitable for AIRS/IRS-assisted wireless systems [25], [37]. As the results, φ_{qk} is picked up from a set of discrete phases to achieve $\varphi_{qk} - \theta_{qk} - \psi_{qk} + \phi_{st} = 0$ [25], [31], [32]. In other words, the ideal phase generated by AIRSs is formulated as

$$\varphi_{qk} = \theta_{qk} + \psi_{qk} - \phi_{st}. \tag{5}$$

It is noteworthy that (5) was used not only in the single-user systems but also in the multiuser systems [19], [23], [38], [39]. Nonetheless, due to the rapid advancement of both computing hardware and software, achieving optimal phase settings in practice is no longer an insurmountable challenge [26], [40]. This is particularly evident with the progress made in deep learning and other optimization algorithms, which enable the realization of optimal phase configurations for AIRSs/IRSs. It should be noted that when AIRSs adjust their phases to optimize the received power at D_t, the received power at $D_{t'}$ ($t \neq t'$) may not reach its maximum potential [23]. Nevertheless, in our pursuit of equitable performance for all users, we assume that the signal-to-interference-plus-noise ratios (SINRs) for all users attain their maximum values within the proposed NOMA-AIRS network. This assumption is commonly employed in the context of AIRS/IRS-aided

---

[5]Notice that the channel gains of S-AIRSs-D_t links can be presented via the sums or matrix/vector [7], [21].

NOMA systems [19], [38]. As a result, (4) becomes

$$y_t = e^{-j\phi_{st}} \Big(\sum_{q=1}^{Q} \sum_{k=1}^{K_q} |h_{qk}||g_{qk}| + |n_{st}| \Big) \sum_{l=1}^{L} \sqrt{\rho_l P_S} x_l + z_t. \tag{6}$$

From the NOMA principles, the tth user (D_t) detects the received messages successively. In particular, it detects and subtracts x_1, x_2, ..., and x_{t-1} of the 1st, 2nd, ..., and the $(t-1)^{th}$ users using successive interference cancellation (SIC). Then, it detects its message x_t. As the results, the SINRs at D_t for detecting and subtracting x_1, x_2, ..., and x_{t-1} and detecting x_t are, respectively, formulated as

$$\lambda_{D_t}^{x_1} = \frac{\left|e^{-j\phi_{st}}\right|^2 \Big(\sum_{q=1}^{Q} \sum_{k=1}^{K_q} |h_{qk}||g_{qk}| + |n_{st}| \Big)^2 \rho_1 P_S}{\left|e^{-j\phi_{st}}\right|^2 \Big(\sum_{q=1}^{Q} \sum_{k=1}^{K_q} |h_{qk}||g_{qk}| + |n_{st}| \Big)^2 \sum_{l=2}^{L} \rho_l P_S + \sigma_t^2}, \tag{7}$$

$$\lambda_{D_t}^{x_2} = \frac{\left|e^{-j\phi_{st}}\right|^2 \Big(\sum_{q=1}^{Q} \sum_{k=1}^{K_q} |h_{qk}||g_{qk}| + |n_{st}| \Big)^2 \rho_2 P_S}{\left|e^{-j\phi_{st}}\right|^2 \Big(\sum_{q=1}^{Q} \sum_{k=1}^{K_q} |h_{qk}||g_{qk}| + |n_{st}| \Big)^2 \sum_{l=3}^{L} \rho_l P_S + \sigma_t^2}, \tag{8}$$

$$\vdots,$$

$$\lambda_{D_t}^{x_t} = \frac{\left|e^{-j\phi_{st}}\right|^2 \Big(\sum_{q=1}^{Q} \sum_{k=1}^{K_q} |h_{qk}||g_{qk}| + |n_{st}| \Big)^2 \rho_t P_S}{\left|e^{-j\phi_{st}}\right|^2 \Big(\sum_{q=1}^{Q} \sum_{k=1}^{K_q} |h_{qk}||g_{qk}| + |n_{st}| \Big)^2 \sum_{l=t+1}^{L} \rho_l P_S + \sigma_t^2}. \tag{9}$$

It is because $\left|e^{-j\phi_{st}}\right|^2 = 1$, (7), (8), ..., and (9) are, respectively, become

$$\lambda_{D_t}^{x_1} = \frac{\mathcal{A}_t^2 \rho_1 P_S}{\mathcal{A}_t^2 \sum_{l=2}^{L} \rho_l P_S + \sigma_t^2}, \tag{10}$$

$$\lambda_{D_t}^{x_2} = \frac{\mathcal{A}_t^2 \rho_2 P_S}{\mathcal{A}_t^2 \sum_{l=3}^{L} \rho_l P_S + \sigma_t^2}, \tag{11}$$

$$\vdots,$$

$$\lambda_{D_t}^{x_t} = \frac{\mathcal{A}_t^2 \rho_t P_S}{\mathcal{A}_t^2 \sum_{l=t+1}^{L} \rho_l P_S + \sigma_t^2}, \tag{12}$$

where $\mathcal{A}_t = \sum_{q=1}^{Q} \sum_{k=1}^{K_q} |h_{qk}||g_{qk}| + |n_{st}|$.

Now, the end-to-end (e2e) SINR at D_t is finally computed as

$$\lambda_{D_t}^{e2e} = \min\left\{ \lambda_{D_t}^{x_1}, \lambda_{D_t}^{x_2}, \ldots, \lambda_{D_t}^{x_t} \right\}, \tag{13}$$

where $\lambda_{D_t}^{x_1}, \lambda_{D_t}^{x_2}, \ldots,$ and $\lambda_{D_t}^{x_t}$ are, respectively, given in (10), (11), ..., and (12).

III. PERFORMANCE ANALYSIS
A. ERGODIC CAPACITY ANALYSIS
The EC at D_t of the proposed NOMA-AIRS network is formulated as

$$\mathcal{E}_{D_t} = \mathbb{E}\left\{ \log_2(1 + \lambda_{D_t}^{e2e}) \right\}. \tag{14}$$

Replacing $\lambda_{D_t}^{e2e}$ from (13) into (14), we have

$$\mathcal{E}_{D_t} = \mathbb{E}\left\{ \log_2 \left[1 + \min\left\{ \lambda_{D_t}^{x_1}, \lambda_{D_t}^{x_2}, \ldots, \lambda_{D_t}^{x_t} \right\} \right] \right\}, \tag{15}$$

Now, (15) can be formulated as

$$\mathcal{E}_{D_t} = \min\left\{ \underbrace{\mathbb{E}\left\{ \log_2\left(1 + \lambda_{D_t}^{x_1}\right) \right\}}_{\mathcal{E}_{D_t}^{x_1}}, \underbrace{\mathbb{E}\left\{ \log_2\left(1 + \lambda_{D_t}^{x_2}\right) \right\}}_{\mathcal{E}_{D_t}^{x_2}}, \ldots, \underbrace{\mathbb{E}\left\{ \log_2\left(1 + \lambda_{D_t}^{x_t}\right) \right\}}_{\mathcal{E}_{D_t}^{x_t}} \right\}. \tag{16}$$

Based on (16), the EC at D_t of the proposed NOMA-AIRS network is obtained as follows.

Theorem: The EC at D_t of the proposed NOMA-AIRS network over realistic Nakagami-m channel is given by

$$\mathcal{E}_{D_t} = \min\{\mathcal{E}_{D_t}^{x_1}, \mathcal{E}_{D_t}^{x_2}, \ldots, \mathcal{E}_{D_t}^{x_t}\}, \tag{17}$$

where

$$\mathcal{E}_{D_t}^{x_1} = \frac{\pi \rho_1}{\Psi \Gamma(\Lambda_t) \ln 2} \sum_{u=1}^{\Psi} \frac{\sqrt{1 - \xi_u^2}}{\rho_1(1 + \xi_u) + 2\sum_{l=2}^{L} \rho_l} \\ \times \Gamma\left(\Lambda_t, \Delta_t \sqrt{\frac{1 + \xi_u}{\bar{\lambda}_{D_t}(1 - \xi_u)\sum_{l=2}^{L} \rho_l}} \right), \tag{18}$$

$$\mathcal{E}_{D_t}^{x_2} = \frac{\pi \rho_2}{\Psi \Gamma(\Lambda_t) \ln 2} \sum_{u=1}^{\Psi} \frac{\sqrt{1 - \xi_u^2}}{\rho_2(1 + \xi_u) + 2\sum_{l=3}^{L} \rho_l} \\ \times \Gamma\left(\Lambda_t, \Delta_t \sqrt{\frac{1 + \xi_u}{\bar{\lambda}_{D_t}(1 - \xi_u)\sum_{l=3}^{L} \rho_l}} \right),$$

$$\vdots \tag{19}$$

$$\mathcal{E}_{D_t}^{x_t} = \frac{\pi \rho_t}{\Psi \Gamma(\Lambda_t) \ln 2} \sum_{u=1}^{\Psi} \frac{\sqrt{1 - \xi_u^2}}{\rho_t(1 + \xi_u) + 2\sum_{l=t+1}^{L} \rho_l} \\ \times \Gamma\left(\Lambda_t, \Delta_t \sqrt{\frac{1 + \xi_u}{\bar{\lambda}_{D_t}(1 - \xi_u)\sum_{l=t+1}^{L} \rho_l}} \right), \tag{20}$$

herein, $\bar{\lambda}_{D_t} = P_S/\sigma_t^2$; Ψ is the Chebyshev parameter; $\xi_u = \cos\left(\frac{(2u-1)\pi}{2\Psi}\right)$; Λ_t and Δ_t, are, respectively, given by

$$\Lambda_t = \frac{[\mu_{\mathcal{A}_t}(1)]^2}{\mu_{\mathcal{A}_t}(2) - [\mu_{\mathcal{A}_t}(1)]^2}, \tag{21}$$

$$\Delta_t = \frac{\mu_{\mathcal{A}_t}(1)}{\mu_{\mathcal{A}_t}(2) - [\mu_{\mathcal{A}_t}(1)]^2}, \tag{22}$$

where $\mu_{\mathcal{A}_t}(1)$ and $\mu_{\mathcal{A}_t}(2)$ are the 1st and 2nd moments of $\mathcal{A}_t$, given in (57) and (58), respectively.

Proof: Since $\mathcal{E}_{D_t}^{x_1}$, $\mathcal{E}_{D_t}^{x_2}$, ..., and $\mathcal{E}_{D_t}^{x_t}$ have a similar form, we will focus on the term $\mathcal{E}_{D_t}^{x_t}$. Mathematically, it is formulated as

$$\mathcal{E}_{D_t}^{x_t} = \mathbb{E}\left\{\log_2\left(1 + \lambda_{D_t}^{x_t}\right)\right\} = \int_0^\infty \log_2(1+y)f_{\lambda_{D_t}^{x_t}}(y)dy$$

$$= \frac{1}{\ln 2}\int_0^\infty \frac{1 - F_{\lambda_{D_t}^{x_t}}(y)}{1+y}dy. \tag{23}$$

To calculate (23), we must compute $F_{\lambda_{D_t}^{x_t}}(y)$ first. Mathematically, it is formulated as

$$F_{\lambda_{D_t}^{x_t}}(y) = \Pr\left\{\lambda_{D_t}^{x_t} < y\right\}. \tag{24}$$

Replacing $\lambda_{D_t}^{x_t}$ from (12) into (24), $F_{\lambda_{D_t}^{x_t}}(y)$ is now formulated as

$$F_{\lambda_{D_t}^{x_t}}(y) = \Pr\left\{\frac{\mathcal{A}_t^2 \rho_t P_S}{\mathcal{A}_t^2 \sum_{l=t+1}^L \rho_l P_S + \sigma_t^2} < y\right\}. \tag{25}$$

Then, we represent (25) as

$$F_{\lambda_{D_t}^{x_t}}(y) = \Pr\left\{\left[\mathcal{A}_t^2 P_S\left(\rho_t - y\sum_{l=t+1}^L \rho_l\right) < \sigma_t^2 y\right]\right\}. \tag{26}$$

From (26), we can obtain $F_{\lambda_{D_t}^{x_t}}(y)$, i.e.,

$$F_{\lambda_{D_t}^{x_t}}(y) = \begin{cases} 1 - \dfrac{1}{\Gamma(\Lambda_t)}\Gamma\left(\Lambda_t, \Delta_t\sqrt{\dfrac{y}{\bar{\lambda}_{D_t}\left(\rho_t - y\sum_{l=t+1}^L \rho_l\right)}}\right) \\ \quad\text{if}\quad y < \dfrac{\rho_t}{\sum_{l=t+1}^L \rho_l}, \\ 1 \quad\text{if}\quad y \geq \dfrac{\rho_t}{\sum_{l=t+1}^L \rho_l}. \end{cases} \tag{27}$$

Replacing (27) into (23), we obtain (20). By applying similar ways, we can derive (18) and (19). The detailed proofs are provided in the Appendix.

Remark 1: It is worth noticing that due to the NOMA principles, the SINR for detecting the final message (x_L) at the Lth user is different to (10), (11), ..., and (12), i.e.,

$$\lambda_{D_L}^{x_L} = \frac{\mathcal{A}_L^2 \rho_L P_S}{\sigma_L^2}. \tag{28}$$

Thus, the final term $\mathcal{E}_{D_L}^{x_L}$ is also different to (18), (19), ..., and (20). Particularly, it is formulated as

$$\mathcal{E}_{D_L}^{x_L} = \frac{2^{\Lambda_L - 1}}{\sqrt{\pi}\,\Gamma(\Lambda_L)\ln 2}G_{3,5}^{5,3}\left(\frac{\Delta_L^2}{4\rho_L\bar{\lambda}_{D_L}}\,\bigg|\,{0, \frac{1}{2}, 1 \atop \frac{\Lambda_L}{2}, \frac{\Lambda_L+1}{2}, 0, \frac{1}{2}, 0}\right). \tag{29}$$

Please refer to the Appendix for more details.

Remark 2: Since the Nakagami-m channels are utilized, the fading order (m) and the average channel gain (Ω) of the channels follow Gamma distributions. More specifically,

the CDF and PDF of channel magnitude, i.e., $|n_{st}|$ are respectively given as [32]

$$F_{|n_{st}|}(y) = \frac{1}{\Gamma(m_{st})}\gamma\left(m_{st}, \frac{m_{st}}{\Omega_{st}}y^2\right)$$

$$= 1 - \frac{1}{\Gamma(m_{st})}\Gamma\left(m_{st}, \frac{m_{st}}{\Omega_{st}}y^2\right), \; y \geq 0, \tag{30}$$

$$f_{|n_{st}|}(y) = \frac{2m_{st}^{m_{st}}}{\Gamma(m_{st})\Omega_{st}^{m_{st}}}y^{2m_{st}-1}\exp\left(-\frac{m_{st}}{\Omega_{st}}y^2\right), \; y \geq 0. \tag{31}$$

Similar to $|n_{st}|$, the fading orders and the average channel gains of $|h_{qk}|$ and $|g_{qk}|$ are denoted by m_{h_q}, m_{g_q}, Ω_{h_q}, and Ω_{g_q}, respectively. Notice that to make our results practically, the realistic Nakagami-m channels are utilized in this paper. In particular, the S-AIRSs and AIRSs-user channels are characterized by the LoS components due to the flexible movements of AIRSs [41], [42]. In the meanwhile, the S-user channels are characterized by non-light-of-sight (NLoS) components due to the blocking objects between S and users [42]. Moreover, the channels recommended to use in 5G & B5G networks are applied, thus, Ω_{h_q} and Ω_{g_q} are, respectively, given as [43]

$$\Omega_{h_q} = G_S - 28 - 20\log(f_c) - 22\log(d_{SI_q}) + G_{I_q}, \tag{32}$$

$$\Omega_{g_q} = G_{I_q} - 28 - 20\log(f_c) - 22\log(d_{I_qD_t}) + G_{D_t}, \tag{33}$$

where G_S, G_{I_q}, and G_{D_t} are the antenna gains of S, the qth AIRS, and D_t, respectively; f_c (in GHz) is the carrier frequency ($2 \leq f_c \leq 6$ GHz); d_{SI_q} and $d_{I_qD_t}$ are the S–q^{th} AIRS and q^{th} AIRS–D_t distances.

In the meanwhile, the NLoS case is utilized for Ω_{st}, i.e.,

$$\Omega_{st} = G_S - 22.7 - 26\log(f_c) - 36.7\log(d_{SD_t}) + G_{D_t}, \tag{34}$$

where d_{SD_t} is the S–D_t distance.[6]

B. ASYMPTOTIC ANALYSIS

In this subsection, we will delve deeper into understanding the system behaviors of the proposed NOMA-AIRS network in the high transmit signal-to-noise (SNR) regime. Our focus will be on analyzing the asymptotic expression of the e2e-SINR at D_t. Particularly, in the high transmit SNR regime, the asymptotic SINRs given in (10), (11), and (12) can be, respectively, formulated as

$$\lim_{\bar{\lambda}_{D_t}\to\infty}\lambda_{D_t}^{x_1} = \lim_{\bar{\lambda}_{D_t}\to\infty}\frac{\mathcal{A}_t^2 \rho_1 P_S}{\mathcal{A}_t^2\sum_{l=2}^L\rho_l P_S + \sigma_t^2}$$

$$= \lim_{\bar{\lambda}_{D_t}\to\infty}\frac{\mathcal{A}_t^2 \rho_1 \bar{\lambda}_{D_t}}{\mathcal{A}_t^2\sum_{l=2}^L\rho_l\bar{\lambda}_{D_t} + 1} = \frac{\rho_1}{\sum_{l=2}^L\rho_l}, \tag{35}$$

---

[6]We should note that the power allocation coefficients in this paper are allocated based on the distances from S to users. Meanwhile, the average channel gains are calculated from these distances as in (32), (33), and (34). In other words, the power allocation coefficients are set based on the average channel gains.

$$\lim_{\bar{\lambda}_{D_t} \to \infty} \lambda_{D_t}^{x_2} = \lim_{\rho \to \infty} \frac{\mathcal{A}_t^2 \rho_2 P_S}{\mathcal{A}_t^2 \sum_{l=3}^{L} \rho_l P_S + \sigma_t^2}$$

$$= \lim_{\rho \to \infty} \frac{\mathcal{A}_t^2 \rho_2 \bar{\lambda}_{D_t}}{\mathcal{A}_t^2 \sum_{l=3}^{L} \rho_l \bar{\lambda}_{D_t} + 1} = \frac{\rho_2}{\sum_{l=3}^{L} \rho_l}, \quad (36)$$

$$\lim_{\bar{\lambda}_{D_t} \to \infty} \lambda_{D_t}^{x_t} = \lim_{\bar{\lambda}_{D_t} \to \infty} \frac{\mathcal{A}_t^2 \rho_t P_S}{\mathcal{A}_t^2 \sum_{l=t+1}^{L} \rho_l P_S + \sigma_t^2}$$

$$= \lim_{\bar{\lambda}_{D_t} \to \infty} \frac{\mathcal{A}_t^2 \rho_t \bar{\lambda}_{D_t}}{\mathcal{A}_t^2 \sum_{l=t+1}^{L} \rho_l \bar{\lambda}_{D_t} + 1} = \frac{\rho_t}{\sum_{l=t+1}^{L}}. \quad (37)$$

Therefore, the asymptotic e2e-SINR at D_t given in (13) is formulated as

$$\lim_{\bar{\lambda}_{D_t} \to \infty} \lambda_{D_t}^{e2e} = \min \left\{ \frac{\rho_1}{\sum_{l=2}^{L} \rho_l}, \frac{\rho_2}{\sum_{l=3}^{L} \rho_l}, \dots, \frac{\rho_t}{\sum_{l=t+1}^{L}} \right\}. \quad (38)$$

As indicated in (38), $\lambda_{D_t}^{e2e}$ at D_t of the proposed NOMA-AIRS network relies on the power allocation coefficients $(\rho_1, \rho_2, \dots,$ and $\rho_L)$ in the high transmit SNR regime. Since $\rho_1, \rho_2, \dots,$ and ρ_L are constants, $\lambda_{D_t}^{e2e}$ at D_t is a constant in the high transmit SNR regime. Consequently, the ECs of the proposed NOMA-AIRS network are also constants in the high transmit SNR regime.

IV. NUMERICAL RESULTS

In this section, the EC behaviors of the proposed NOMA-AIRS network are deeply investigated. Besides simulations of the ECs of the proposed NOMA-AIRS network to confirm the exactness of the derived expressions, we also provide the ECs of the conventional NOMA network without AIRS (denoted by "D_t-No-AIRS" in the below figures) to clarify the benefits of utilizing AIRSs. Unless otherwise stated, we set $L = 3$ users, $Q = 4$ AIRSs, $\sigma_1^2 = \sigma_2^2 = \sigma_3^2 = \sigma^2$, and $m_{st} = m_{h_q} = m_{g_q} = m$. In addition, the practical parameters are chosen when determining the EC behaviors of the proposed NOMA-AIRS network, i.e., $B_w = 10$ MHz, $N_f = 10$ dBm, and $N_0 = -174$ dBm/Hz (for calculating σ^2 given in (2)) [7], [25], [44]. To obtain the average channel gains from (32), (33), and (34), we set $G_S = G_{I_q} = G_{D_t} = 5$ dB while the carrier frequency and distance are varied. In particular, the locations of S, AIRSs, and users are expressed by using 3D coordinates (x, y, z) where the locations of S and three users are fixed, i.e., $(x_S, y_S, z_S) = (0, 0, 10)$, $(x_{D_1}, y_{D_1}, z_{D_1}) = (100, 5, 10)$, $(x_{D_2}, y_{D_2}, z_{D_2}) = (90, 8, 10)$, and $(x_{D_3}, y_{D_3}, z_{D_3}) = (80, 6, 10)$.[7] The x- and y-axes of AIRSs are set unchangingly, e.g., $(x_{AIRS_1}, y_{AIRS_1}) = (10, 20)$, $(x_{AIRS_2}, y_{AIRS_2}) = (30, 15)$, $(x_{AIRS_3}, y_{AIRS_3}) = (50, 10)$, and $(x_{AIRS_4}, y_{AIRS_4}) = (60, 15)$ while the z-axes of AIRSs can be varied. For reading convenience, the system parameters are detailedly listed in Tab. 2.

---

[7] The distance between two nodes, i.e., S and D_1 is computed as $d_{SD_1} = \sqrt{(x_{D_1} - x_S)^2 + (y_{D_1} - y_S)^2 + (z_{D_1} - z_S)^2}$.

TABLE 2. System parameters.

| Notation	Fixed value	Varying range
P_S dBm	5	$0 \sim 30$
Q AIRSs	4	none
L users	3	none
G_S, G_{I_q}, G_{D_t} dB	5	none
B_w MHz	10	$1 \sim 10$
N_f dBm	10	none
N_0 dBm/Hz	-174	none
K_q REs	20	10, 15, 25
$\sum K_q$ REs	80	40, 60, 100
ρ_1, ρ_2, ρ_3	0.6, 0.3, 0.1	none
(x_S, y_S, z_S)	$(0, 0, 10)$	none
$(x_{D_1}, y_{D_1}, z_{D_1})$	$(100, 5, 10)$	none
$(x_{D_2}, y_{D_2}, z_{D_2})$	$(90, 8, 10)$	none
$(x_{D_3}, y_{D_3}, z_{D_3})$	$(80, 6, 10)$	none
(x_{AIRS_1}, y_{AIRS_1})	$(10, 20)$	none
(x_{AIRS_2}, y_{AIRS_2})	$(30, 15)$	none
(x_{AIRS_3}, y_{AIRS_3})	$(50, 10)$	none
(x_{AIRS_4}, y_{AIRS_4})	$(60, 15)$	none
z_{AIRS_1}	140	150, 200, 250
z_{AIRS_2}	150	140, 200, 250
z_{AIRS_3}	200	150, 170, 250
z_{AIRS_4}	180	150, 200, 250
m	2	1
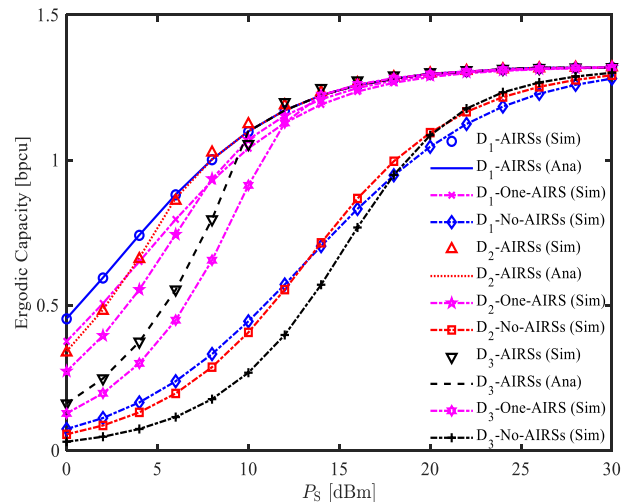
FIGURE 2. The ECs of the proposed NOMA-AIRS network with $z_{AIRS_1} = 200$, $z_{AIRS_2} = 140$, $z_{AIRS_3} = 150$, $z_{AIRS_4} = 180$, $K_1 = K_2 = K_3 = K_4 = 20$ REs, $f_c = 5$ GHz, $B_w = 10$ MHz, and $m = 2$.

Fig. 2 illustrates the ECs of the proposed NOMA-AIRS network with $z_{AIRS_1} = 200$, $z_{AIRS_2} = 140$, $z_{AIRS_3} = 150$, $z_{AIRS_4} = 180$, $K_1 = K_2 = K_3 = K_4 = 20$ REs, $f_c = 5$ GHz, and $m = 2$. The EC analytical curves of the proposed NOMA-AIRS network are achieved by using (17) where the terms $\mathcal{E}_{D_1}^{x_1}, \mathcal{E}_{D_2}^{x_1}$, and $\mathcal{E}_{D_3}^{x_1}$ are obtained by using (18); $\mathcal{E}_{D_1}^{x_2}, \mathcal{E}_{D_2}^{x_2}$, and $\mathcal{E}_{D_3}^{x_2}$ are obtained by using (19); $\mathcal{E}_{D_1}^{x_3}$ and $\mathcal{E}_{D_2}^{x_3}$ are obtained by using (20) while and $\mathcal{E}_{D_3}^{x_3}$ is obtained by using (29). It is obvious in Fig. 2 that the ECs of the proposed NOMA-AIRS network (denoted by "D_t-AIRSs") are dramatically

higher than those of the conventional NOMA network without AIRSs (denoted by "D_t-No-AIRSs"). Moreover, the ECs of NOMA network with only one AIRS (denoted by "D_t-One-AIRS"), computed based on previous works [27], [28], are also provided to confirm the benefits of the proposed network. To ensure a fair comparison, we align the parameters with those used in [27] and [28]. Specifically, we configure the system with $Q = 1$ AIRS and $K = 80$ REs to obtain ECs in the case of utilizing only one AIRS. In essence, the total number of REs in [27] and [28] and this paper remains consistent. Additionally, the coordinate of this AIRS is defined as $(x_{\text{AIRS}}, y_{\text{AIRS}}, z_{\text{AIRS}}) = (30, 15, 180)$. In particular, at $P_S = 6$ dBm, the ECs at D_1, D_2, and D_3 are, respectively 0.88, 0.87, and 0.55 bits per channel use (bpcu) corresponding to the proposed NOMA-AIRS network while they are, respectively only 0.24, 0.2, and 0.12 bpcu corresponding to the conventional NOMA network. These results confirm the big advantages of utilizing AIRSs for improving the capacity of the NOMA networks. An important observation is that the advantages of utilizing AIRSs depend on the transmit power of S. More specifically, the big advantages of utilizing AIRSs are clear when $P_S < 30$ dBm. However, due to the NOMA features, the ECs of the proposed NOMA-AIRS network and the conventional NOMA network will be similar when $P_S > 30$ dBm. In other words, we should use suitable P_S to exploit the advantages of AIRSs in the NOMA networks.[8]

Fig. 3 determines the effects of distributed AIRSs on the ECs of the proposed NOMA-AIRS network. In particular, the z-axes of 4 AIRSs are $z_{\text{AIRS}_1} = 140$, $z_{\text{AIRS}_2} = 170$, $z_{\text{AIRS}_3} = 200$, $z_{\text{AIRS}_4} = 200$ and the total number of REs is fixed, i.e., $K_1 + K_2 + K_3 + K_4 = 80$ REs. It is worth noticing that with these position settings, AIRS_1 is the nearest AIRS from S. Three cases are investigated, i.e., $\mathbf{K} = [K_1 \ K_2 \ K_3 \ K_4] = [25 \ 25 \ 20 \ 10]$, $\mathbf{K} = [K_1 \ K_2 \ K_3 \ K_4] = [20 \ 20 \ 20 \ 20]$, and $\mathbf{K} = [K_1 \ K_2 \ K_3 \ K_4] = [10 \ 20 \ 25 \ 25]$. We observe that the case of $\mathbf{K} = [K_1 \ K_2 \ K_3 \ K_4] = [25 \ 25 \ 20 \ 10]$ is the best case among three considered cases. This result fits in with the feature of distributed IRSs [7], [32]. Therefore, when multiple AIRSs are utilized to aid NOMA networks, the AIRSs with larger sizes should be nearer the transmitter for better reflecting signals to users.

Fig. 4 investigates the impacts of f_c on the ECs of the proposed NOMA-AIRS network and the conventional NOMA network with $z_{\text{AIRS}_1} = 140$, $z_{\text{AIRS}_2} = 170$, $z_{\text{AIRS}_3} = 200$, $z_{\text{AIRS}_4} = 200$, $\mathbf{K} = [25 \ 25 \ 20 \ 10]$, and $m = 2$. Two carrier frequencies are utilized, i.e.,

FIGURE 3. The ECs of the proposed NOMA-AIRS network with $z_{\text{AIRS}_1} = 140$, $z_{\text{AIRS}_2} = 170$, $z_{\text{AIRS}_3} = 200$, $z_{\text{AIRS}_4} = 200$, $f_c = 5$ GHz, $B_W = 10$ MHz, and $m = 2$.
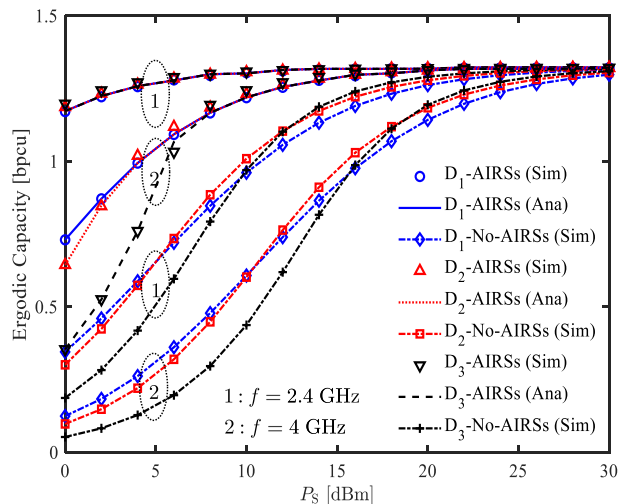
FIGURE 4. The ECs of the proposed NOMA-AIRS network with $z_{\text{AIRS}_1} = 140$, $z_{\text{AIRS}_2} = 170$, $z_{\text{AIRS}_3} = 200$, $z_{\text{AIRS}_4} = 200$, $\mathbf{K} = [25 \ 25 \ 20 \ 10]$, $B_W = 10$ MHz, and $m = 2$.

$f_c = 2.4$ and $f_c = 4$ GHz.[9] It is clear that the impacts of f_c on the ECs of the proposed NOMA-AIRS network and the conventional NOMA network are significant. On the other hand, with $f_c = 2.4$ GHz, the ECs of the three users of the proposed NOMA-AIRS network are nearly similar in Fig. 4 while they are greatly different in Fig. 3. Particularly, at $P_S = 5$ dBm, when f_c increases from 2.4 GHz to 4 GHz, the ECs at D_1 and D_2 of the proposed NOMA-AIRS network reduce from 1.27 bpcu to 1 bpcu while the EC at D_3 reduces from 1.27 bpcu to 0.76 bpcu. In other words, when the system configurations are fixed, an increase in f_c

---

[8] We observe that with these power allocation coefficients ($\rho_1 = 0.6$, $\rho_2 = 0.3$, and $\rho_3 = 0.1$), the ECs at D_1, D_2, and D_3 are similar when $P_S > 10$ dBm. In other words, with these settings, we obtain fairness for all users in the proposed NOMA-AIRS network. Notably, the power allocation coefficients can be set as $\rho_l = (L - l + 1)/\mathcal{L}$, where $\mathcal{L}$ is to ensure $\sum_{l=1}^{K} \rho_l = 1$ [45]. Therefore, we can set $\rho_1 = 1/2$, $\rho_2 = 1/3$, and $\rho_3 = 1/6$. However, these values are also not optimal because it is too difficult to optimize the power allocation coefficients with $L \geq 3$ [17], [19], [23], [45]. As a result, the optimization issues can be considered as our future works.
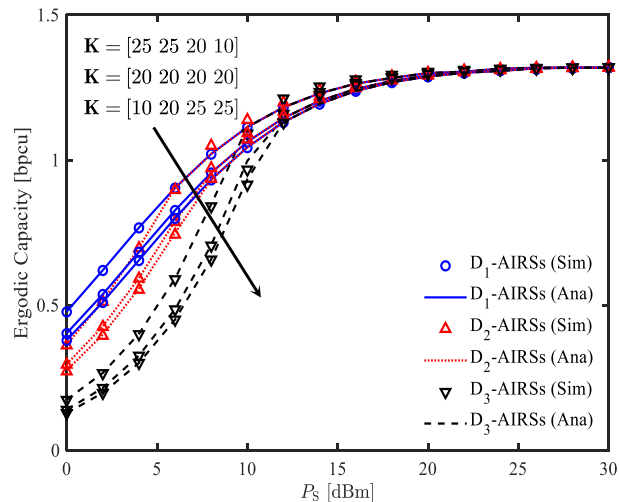
[9] In practice, the Wi-Fi networks use $f_c = 2.4$ and $f_c = 5$ GHz. Since the case that $f_c = 5$ GHz was investigated in the previous figures, we consider the case that $f_c = 4$ GHz in Fig. 4 to achieve more behaviors of the proposed NOMA-AIRS network.
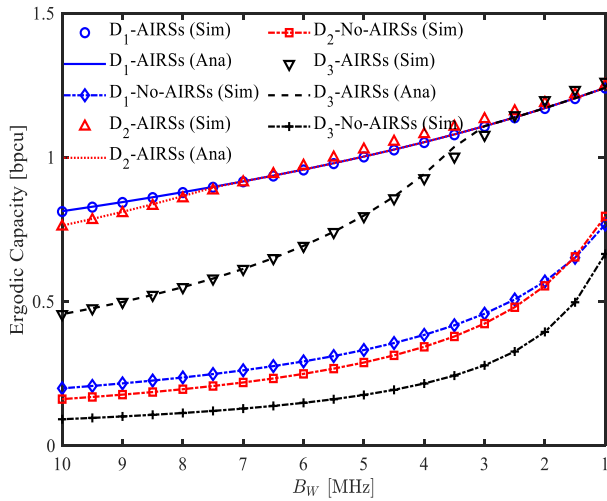
FIGURE 5. The effects of B_W on the ECs of the proposed NOMA-AIRS network with $P_S = 5$ dBm, $z_{AIRS_1} = 200$, $z_{AIRS_2} = 140$, $z_{AIRS_3} = 150$, $z_{AIRS_4} = 180$, $K_1 = K_2 = K_3 = K_4 = 20$ REs, $f_c = 5$ GHz, and $m = 2$.
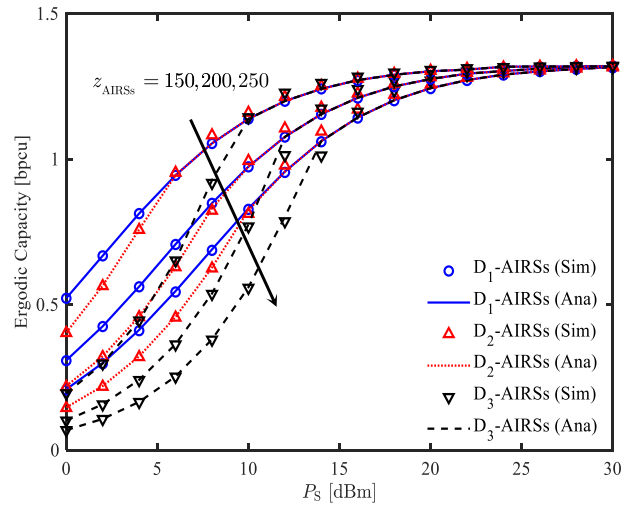

FIGURE 6. The ECs of the proposed NOMA-AIRS network with $K_1 = K_2 = K_3 = K_4 = 20$ REs, $f_c = 5$ GHz, $B_W = 10$ MHz, and $m = 2$.
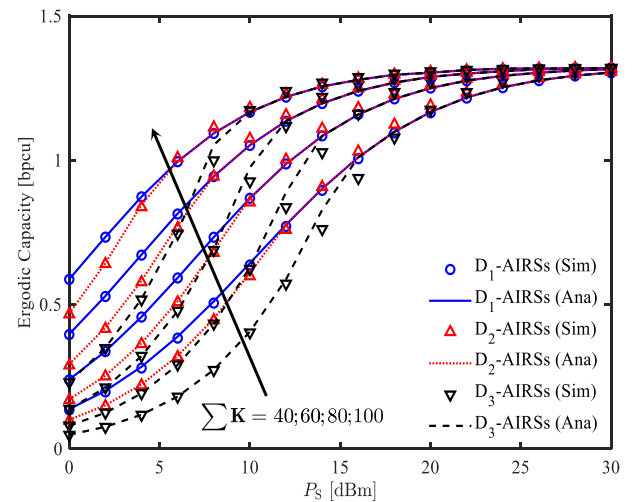

FIGURE 7. The ECs of the proposed NOMA-AIRS network for different totals of REs with $z_{AIRS_1} = 200$, $z_{AIRS_2} = 140$, $z_{AIRS_3} = 150$, $z_{AIRS_4} = 180$, $f_c = 5$ GHz, $B_W = 10$ MHz, and $m = 1$.

will dramatically reduce the ECs of the proposed NOMA-AIRS network. Similar to the ECs of the proposed NOMA-AIRS network, the ECs of the conventional NOMA network are also dramatically reduced with f_c. Moreover, the reduction at D_3 is dramatically bigger than that at D_1 and D_2 when f_c increases. Hence, employing suitable frequency allocations proves to be an efficient approach for boosting the capacity of NOMA networks.

Fig. 5 plots the ECs of the proposed NOMA-AIRS network and the conventional NOMA network versus the bandwidth B_w with $P_S = 5$ dBm, $z_{AIRS_1} = 200$, $z_{AIRS_2} = 140$, $z_{AIRS_3} = 150$, $z_{AIRS_4} = 180$, $K_1 = K_2 = K_3 = K_4 = 20$ REs, $f_c = 5$ GHz, and $m = 2$. As can be seen in Fig. 5, the ECs of the proposed NOMA-AIRS network and the conventional NOMA network increase when B_w decreases. This result matches with the mathematical model presented in (2). It is because an increase in B_w will increase the variance of Gaussian noise. In particular, the ECs at D_1, D_2, and D_3 of the proposed NOMA-AIRS network increase from 0.8, 0.76, and 0.46 bpcu at $B_w = 10$ MHz to 1.02, 1.0, and 0.8 bpcu at $B_w = 5$ MHz. When B_w continuously reduces, the ECs of the proposed NOMA-AIRS network and the conventional NOMA network will be enhanced. As a result, suitable B_w should be utilized to satisfy the system requirements and reduce the noise power at the users.

Fig. 6 depicts the ECs of the proposed NOMA-AIRS network where the altitudes of the AIRSs are varied, i.e., $z_{AIRS_1} = z_{AIRS_2} = z_{AIRS_3} = z_{AIRS_4} = z_{AIRSs} = 150, 200$, and 250. Since the higher altitudes of the AIRSs lead to higher distances between S and AIRSs and between AIRSs and users, the EC of the proposed NOMA-AIRS network is significantly reduced with z_{AIRSs}. Particularly, the EC at D_1 reduces from 0.94 to 0.71 and 0.55 bpcu when z_{AIRSs} increases from 150 to 200 and 250, respectively. In other words, when z_{AIRSs} is 50 higher, the EC at D_1 decreases

approximately 0.2 bpcu. Similar to D_1, the ECs at D_2 and D_3 are considerably reduced when z_{AIRSs} increases.

Fig. 7 illustrates the benefits of utilizing AIRSs in the proposed NOMA-AIRS network where the totals of REs are changed, i.e., $\sum K_q = 40, 60, 80$, and 100 REs. In other words, we consider four cases, i.e., $K_1 = K_2 = K_3 = K_4 = 10$, $K_1 = K_2 = K_3 = K_4 = 15$, $K_1 = K_2 = K_3 = K_4 = 20$, and $K_1 = K_2 = K_3 = K_4 = 25$ REs. As shown in Fig. 7, when the total of REs is 20 REs higher, the ECs of the proposed NOMA-AIRS network are greatly increased. In particular, the ECs at D_1, D_2, and D_3 increase from 0.64, 0.63, and 0.41 to 0.87, 0.86, and 0.63 bpcu when $\sum K_q$ increases from 40 to 60 REs. When $\sum K_q$ continuously increases, the ECs of the proposed NOMA-AIRS network will be dramatically increased. However, when the transmit power is high enough, i.e., $P_S = 30$ dBm, the ECs with $\sum K_q = 40, 60, 80$, and 100 REs are similar due to the

NOMA features. Therefore, to exploit the huge benefits of the AIRSs, a suitable transmit power should be used in the proposed NOMA-AIRS network.

From the behaviors of the proposed NOMA-AIRS network obtained in Fig. 2–Fig. 7, we observe that the EC is intricately shaped by the interplay of key factors. More specifically, the transmit power of S in coordination with the density and deployment of REs, assumes a central role in defining the system's achievable capacity. The usage of high transmit power is not a good solution for improving the EC of the proposed NOMA-AIRS network due to the saturated ceiling. In addition, the strategic placement of AIRS elements can considerably elevate the system's capacity. Concurrently, it is important to choose suitable carrier frequency and bandwidth for utilizing in the proposed network. When the carrier frequency is higher, we can use larger sizes of AIRSs to maintain the EC. Furthermore, the cumulative count of REs introduces a trade-off between heightened complexity and improved performance. This complex synergy of transmit power, number of REs, AIRS placement, carrier frequency, bandwidth, and total REs underscores the holistic approach essential for comprehending and optimizing the EC of the proposed NOMA-AIRS network.

V. CONCLUSION

This paper exploited the advantages of multiple AIRSs to improve the capacity of the NOMA network over realistic Nakagami-m channels. In particular, Q AIRSs were deployed to aid L users adopting NOMA schemes. The EC expressions at users of the proposed NOMA-AIRS network were obtained using the 5G & B5G channel model. Based on the obtained expressions, the EC behaviors of the proposed NOMA-AIRS network were thoroughly determined. Numerical results confirmed the advantages of utilizing AIRSs in NOMA networks. Particularly, the ECs of the proposed NOMA-AIRS network are significantly higher than the ECs of the conventional NOMA network (without AIRSs). More specifically, utilizing 4 AIRSs where each AIRS has 20 REs, the ECs of the proposed NOMA-AIRS network can be two times higher than those of the conventional NOMA network. However, in the high transmit power regime, the benefits of utilizing AIRSs are reduced due to the NOMA features. In addition, the effects of number of REs and total of REs in the AIRSs, bandwidth, altitudes of AIRSs, and carrier frequency used in Wi-Fi systems were deeply determined. From these observations, some recommendations were suggested to enhance the EC performance of the proposed NOMA-AIRS network in practice. To further improve the performance of the proposed NOMA-AIRS network, some solutions such as optimization of the AIRSs' trajectory, resource allocation in the NOMA scheme, utilizing multi-antenna, and applying deep/machine learning can be continuously performed. We let them for our future works.

APPENDIX

This appendix provides all mathematical calculations to obtain the ECs of the proposed NOMA-AIRS network given in (17), (18), (19), and (20). In particular, before deriving these formulas, we firstly derive $F_{\lambda_{\mathrm{D}_t}^{x_t}}(y)$ in (27) and then use it to compute EC. Since $\mathcal{A}_t = \sum_{q=1}^{Q} \sum_{k=1}^{K_q} |h_{qk}||g_{qk}| + |n_{st}|$, the moments of $|n_{st}|$ and $\sum_{q=1}^{Q} \sum_{k=1}^{K_q} |h_{qk}||g_{qk}|$ have to be derived to compute the moments of $\mathcal{A}_t$.

First, the βth moment of $|n_{st}|$ is given as

$$\mu_{|n_{st}|}(\beta) \triangleq \mathbb{E}\{|n_{st}|^{\beta}\} = \int_0^{\infty} y^{\beta} f_{|n_{st}|}(y) dy. \quad (39)$$

Using (31) and applying [46, Eq. (3.461.3)], (39) now is expressed as

$$\mu_{|n_{st}|}(\beta) = \frac{\Gamma(m_{st} + \beta/2)}{\Gamma(m_{st})} \left(\frac{m_{st}}{\Omega_{st}}\right)^{-\beta/2}, \quad (40)$$

where Ω_{st} is detailedly presented in the Remark 2.

From (40), we have

$$\mu_{|n_{st}|}(1) = \frac{\Gamma(m_{st} + 1/2)}{\Gamma(m_{st})} \times \sqrt{\frac{\Omega_{st}}{m_{st}}}, \quad (41)$$

$$\mu_{|n_{st}|}(2) = \frac{\Gamma(m_{st} + 1)}{\Gamma(m_{st})} \times \frac{\Omega_{st}}{m_{st}} = \Omega_{st}. \quad (42)$$

To derive the moments of $\mathcal{A}_t$, let $\mathcal{B}_{qk} = |h_{qk}||g_{qk}|$, $\mathcal{C}_q = \sum_{k=1}^{K_q} \mathcal{B}_{qk}$, and $\mathcal{H}_t = \sum_{q=1}^{Q} \mathcal{C}_q$ be new variables. Consequently, $\mathcal{A}_t = \mathcal{H}_t + |n_{st}|$. Now, the PDF of $\mathcal{B}_{qk} = |h_{qk}||g_{qk}|$ is

$$f_{\mathcal{B}_{qk}}(y) = \int_0^{\infty} \frac{1}{x} f_{|h_{qk}|}\left(\frac{y}{x}\right) f_{|g_{qk}|}(x) dx. \quad (43)$$

Using (31), (43) now is expressed as

$$f_{\mathcal{B}_{qk}}(y) = \frac{4}{\Gamma(m_{h_q})\Gamma(m_{g_q})} \left(\frac{m_{h_q}}{\Omega_{h_q}}\right)^{m_{h_q}} \left(\frac{m_{g_q}}{\Omega_{g_q}}\right)^{m_{g_q}}$$
$$\times y^{2m_{h_q}-1} \int_0^{\infty} x^{2m_{g_q}-2\,m_{h_q}-1}$$
$$\times \exp\left(-\frac{m_{h_q}y^2}{\Omega_{h_q}x^2} - \frac{m_{g_q}x^2}{\Omega_{g_q}}\right) dx. \quad (44)$$

Using [46, Eq. (3.478.4)], (44) becomes

$$f_{\mathcal{B}_{qk}}(y) = \frac{4}{\Gamma(m_{h_q})\Gamma(m_{g_q})} \left(\frac{m_{h_q}m_{g_q}}{\Omega_{h_q}\Omega_{g_q}}\right)^{\frac{m_{h_q}+m_{g_q}}{2}}$$
$$\times y^{m_{h_q}+m_{g_q}-1} \mathcal{K}_{m_{g_q}-m_{h_q}}\left(2y\sqrt{\frac{m_{h_q}m_{g_q}}{\Omega_{h_q}\Omega_{g_q}}}\right). \quad (45)$$

Now, we can compute the βth moment of $\mathcal{B}_{qk}$, i.e.,

$$\mu_{\mathcal{B}_{qk}}(\beta) \triangleq \mathbb{E}\{\mathcal{B}_{qk}^{\beta}\} = \int_0^{\infty} y^{\beta} f_{\mathcal{B}_{qk}}(y) dy. \quad (46)$$

Substituting (45) into (46) and applying [46, Eq. (6.561.16)], (46) is solved as

$$\mu_{\mathcal{B}_{qk}}(\beta) = \left(\frac{m_{h_q}m_{g_q}}{\Omega_{h_q}\Omega_{g_q}}\right)^{\frac{-\beta}{2}} \times \frac{\Gamma(m_{h_q} + \beta/2)\Gamma(m_{g_q} + \beta/2)}{\Gamma(m_{h_q})\Gamma(m_{g_q})}. \quad (47)$$

Then, the moments of $\mathcal{B}_{qk}$ are specific as

$$\mu_{\mathcal{B}_{qk}}(1) = \sqrt{\frac{\Omega_{h_q}\Omega_{g_q}}{m_{h_q}m_{g_q}}} \times \frac{\Gamma(m_{h_q}+1/2)\Gamma(m_{g_q}+1/2)}{\Gamma(m_{h_q})\Gamma(m_{g_q})}, \quad (48)$$

$$\mu_{\mathcal{B}_{qk}}(2) = \Omega_{h_q}\Omega_{g_q}. \quad (49)$$

As a result, we can obtain the CDF of $\mathcal{B}_{qk}$ from its moments [47], i.e.,

$$F_{\mathcal{B}_{qk}}(y)$$
$$= \frac{1}{\Gamma\left(\frac{[\mu_{\mathcal{B}_{qk}}(1)]^2}{\mu_{\mathcal{B}_{qk}}(2)-[\mu_{\mathcal{B}_{qk}}(1)]^2}\right)}$$
$$\times \gamma\left(\frac{[\mu_{\mathcal{B}_{qk}}(1)]^2}{\mu_{\mathcal{B}_{qk}}(2)-[\mu_{\mathcal{B}_{qk}}(1)]^2}, \frac{\mu_{\mathcal{B}_{qk}}(1)y}{\mu_{\mathcal{B}_{qk}}(2)-[\mu_{\mathcal{B}_{qk}}(1)]^2}\right). \quad (50)$$

Now, the CDF of $\mathcal{C}_q = \sum_{k=1}^{K_q}\mathcal{B}_{qk}$ is computed as

$$F_{\mathcal{C}_q}(y)$$
$$= \frac{1}{\Gamma\left(\frac{K_q[\mu_{\mathcal{B}_{qk}}(1)]^2}{\mu_{\mathcal{B}_{qk}}(2)-[\mu_{\mathcal{B}_{qk}}(1)]^2}\right)}$$
$$\times \gamma\left(\frac{K_q[\mu_{\mathcal{B}_{qk}}(1)]^2}{\mu_{\mathcal{B}_{qk}}(2)-[\mu_{\mathcal{B}_{qk}}(1)]^2}, \frac{\mu_{\mathcal{B}_{qk}}(1)y}{\mu_{\mathcal{B}_{qk}}(2)-[\mu_{\mathcal{B}_{qk}}(1)]^2}\right). \quad (51)$$

Based on [48], we can derive the βth moment of $\mathcal{C}_q$, i.e.,

$$\mu_{\mathcal{C}_q}(\beta) \triangleq \mathbb{E}\{\mathcal{C}_q^\beta\}$$
$$= \sum_{\beta_1=0}^{\beta}\sum_{\beta_2=0}^{\beta_1}\cdots\sum_{\beta_{K_q-1}=0}^{\beta_{K_q-2}}\binom{\beta}{\beta_1}\binom{\beta_1}{\beta_2}\cdots\binom{\beta_{K_q-2}}{\beta_{K_q-1}}$$
$$\times \mu_{\mathcal{B}_{q1}}(\beta-\beta_1)\mu_{\mathcal{B}_{q2}}(\beta_1-\beta_2)\cdots\mu_{\mathcal{B}_{qK_q}}(\beta_{K_q-1}), \quad (52)$$

where $\binom{M}{n} = \frac{M!}{n!(M-n)!}$.

Now, the moment of $\mathcal{H}_t = \sum_{q=1}^{Q}\mathcal{C}_q$ can be computed, i.e.,

$$\mu_{\mathcal{H}_t}(\beta) \triangleq \mathbb{E}\{\mathcal{H}_t^\beta\}$$
$$= \sum_{\beta_1=0}^{\beta}\sum_{\beta_2=0}^{\beta_1}\cdots\sum_{\beta_{Q-1}=0}^{\beta_{Q-2}}\binom{\beta}{\beta_1}\binom{\beta_1}{\beta_2}\cdots\binom{\beta_{Q-2}}{\beta_{Q-1}}$$
$$\times \mu_{\mathcal{C}_1}(\beta-\beta_1)\mu_{\mathcal{C}_2}(\beta_1-\beta_2)\cdots\mu_{\mathcal{C}_Q}(\beta_{Q-1}). \quad (53)$$

Based on (47), (52), and (53), the specific moments of $\mathcal{H}_t$ can be derived, i.e.,

$$\mu_{\mathcal{H}_t}(1)$$
$$= \sum_{q=1}^{Q}\sum_{k=1}^{K_q}\mu_{\mathcal{B}_{qk}}(1), \quad (54)$$

$$\mu_{\mathcal{H}_t}(2)$$
$$= \sum_{q=1}^{Q}\left[\sum_{k=1}^{K_q}\mu_{\mathcal{B}_{qk}}(2) + 2\sum_{k=1}^{K_q}\mu_{\mathcal{B}_{qk}}(1)\sum_{k'=k+1}^{K_q}\mu_{\mathcal{B}_{qk'}}(1)\right]$$
$$+ 2\sum_{q=1}^{Q}\left[\sum_{k=1}^{K_q}\mu_{\mathcal{B}_{qk}}(1)\right]\sum_{q'=q+1}^{Q}\left[\sum_{k=1}^{K_{q'}}\mu_{\mathcal{B}_{q'k}}(1)\right]. \quad (55)$$

Since $\mathcal{H}_t$ and $|n_{st}|$ are independent, the moment of $\mathcal{A}_t = \mathcal{H}_t + |n_{st}|$ is formulated as

$$\mu_{\mathcal{A}_t}(\beta) \triangleq \mathbb{E}\{(\mathcal{H}_t + |n_{st}|)^\beta\} = \mathbb{E}\left\{\sum_{i=0}^{\beta}\binom{\beta}{i}|n_{st}|^i\mathcal{H}_t^{\beta-i}\right\}$$
$$= \sum_{i=0}^{\beta}\binom{\beta}{i}\mu_{|n_{st}|}(i)\mu_{\mathcal{H}_t}(\beta-i). \quad (56)$$

Then, the specific moments of $\mathcal{A}_t$ can be clarified from (56), i.e.,

$$\mu_{\mathcal{A}_t}(1) = \mu_{\mathcal{H}_t}(1) + \mu_{|n_{st}|}(1), \quad (57)$$
$$\mu_{\mathcal{A}_t}(2) = \mu_{\mathcal{H}_t}(2) + \mu_{|n_{st}|}(2) + 2\mu_{\mathcal{H}_t}(1)\mu_{|n_{st}|}(1). \quad (58)$$

As a result, we obtain the CDF of $\mathcal{A}_t$ as

$$F_{\mathcal{A}_t}(y) = \frac{1}{\Gamma\left(\frac{[\mu_{\mathcal{A}_t}(1)]^2}{\mu_{\mathcal{A}_t}(2)-[\mu_{\mathcal{A}_t}(1)]^2}\right)}$$
$$\times \gamma\left(\frac{[\mu_{\mathcal{A}_t}(1)]^2}{\mu_{\mathcal{A}_t}(2)-[\mu_{\mathcal{A}_t}(1)]^2}, \frac{\mu_{\mathcal{A}_t}(1)y}{\mu_{\mathcal{A}_t}(2)-[\mu_{\mathcal{A}_t}(1)]^2}\right)$$
$$= \frac{1}{\Gamma(\Lambda_t)}\gamma(\Lambda_t, \Delta_t y). \quad (59)$$

Now, we can calculate $F_{\lambda_{D_t}^{x_t}}(y)$ from (26). In particular, when $\rho_t - y\sum_{l=t+1}^{L}\rho_l \leq 0$ or $y \geq \frac{\rho_t}{\sum_{l=t+1}^{L}\rho_l}$, (26) is always true because $\mathcal{A}_t^2 P_S\left(\rho_t - y\sum_{l=t+1}^{L}\rho_l\right) \leq 0$ while $\sigma_t^2 y > 0$. In other words, $F_{\lambda_{D_t}^{x_t}}(y) = 1$ with $y \geq \frac{\rho_t}{\sum_{l=t+1}^{L}\rho_l}$. When $\rho_t - y\sum_{l=t+1}^{L}\rho_l > 0$ or $y < \frac{\rho_t}{\sum_{l=t+1}^{L}\rho_l}$, (26) is equivalent to

$$F_{\lambda_{D_t}^{x_t}}(y) = \Pr\left\{\mathcal{A}_t^2 < \frac{\sigma_t^2 y}{P_S\left(\rho_t - y\sum_{l=t+1}^{L}\rho_l\right)}\right\}$$
$$= \Pr\left\{\mathcal{A}_t^2 < \frac{y}{\bar{\lambda}_{D_t}\left(\rho_t - y\sum_{l=t+1}^{L}\rho_l\right)}\right\}. \quad (60)$$

It is because

$$\Pr\{\mathcal{A}_t^2 < X\} = F_{\mathcal{A}_t^2}(X) = F_{\mathcal{A}_t}(\sqrt{X}), \quad (61)$$

(60) can be expressed as

$$F_{\lambda_{D_t}^{x_t}}(y) = \Pr\left\{\mathcal{A}_t < \sqrt{\frac{y}{\bar{\lambda}_{D_t}\left(\rho_t - y\sum_{l=t+1}^{L}\rho_l\right)}}\right\}$$
$$= F_{\mathcal{A}_t}\left(\sqrt{\frac{y}{\bar{\lambda}_{D_t}\left(\rho_t - y\sum_{l=t+1}^{L}\rho_l\right)}}\right). \quad (62)$$

From (59), (61) is now formulated as

$$F_{\lambda_{D_t}^{x_t}}(y) = \frac{1}{\Gamma(\Lambda_t)}\gamma\left(\Lambda_t, \Delta_t\sqrt{\frac{y}{\bar{\lambda}_{D_t}\left(\rho_t - y\sum_{l=t+1}^L \rho_l\right)}}\right).$$
(63)

Combining two above cases, i.e., $y < \frac{\rho_t}{\sum_{l=t+1}^L \rho_l}$ and $y \geq \frac{\rho_t}{\sum_{l=t+1}^L \rho_l}$ and using equation $\Gamma(A, x) + \gamma(A, x) = \Gamma(A)$, we obtain $F_{\lambda_{D_t}^{x_t}}(y)$ as presented in (27). Now, replacing (27) into (23), we have

$$\mathcal{E}_{D_t}^{x_t} = \frac{1}{\Gamma(\Lambda_t)\ln 2}\int_0^{\frac{\rho_t}{\sum_{l=t+1}^L \rho_l}}\frac{1}{1+y}$$
$$\times \Gamma\left(\Lambda_t, \Delta_t\sqrt{\frac{y}{\bar{\lambda}_{D_t}\left(\rho_t - y\sum_{l=t+1}^L \rho_l\right)}}\right)dy. \quad (64)$$

Applying [49, Eq. (25.4.30)], (64) becomes

$$\mathcal{E}_{D_t}^{x_t} = \frac{\pi\rho_t}{2\Psi\sum_{l=t+1}^L \rho_l\Gamma(\Lambda_t)\ln 2}\sum_{u=1}^{\Psi}\frac{\sqrt{1-\xi_u^2}}{1+\frac{\rho_t(1+\xi_u)}{2\sum_{l=t+1}^L \rho_l}}$$
$$\times \Gamma\left(\Lambda_t, \Delta_t\sqrt{\frac{\frac{\rho_t(1+\xi_u)}{2\sum_{l=t+1}^L \rho_l}}{\bar{\lambda}_{D_t}\left(\rho_t - \frac{\rho_t(1+\xi_u)}{2\sum_{l=t+1}^L \rho_l}\sum_{l=t+1}^L \rho_l\right)}}\right).$$
(65)

After some simple transforms, (65) becomes (20). By applying similar steps, we obtain $\mathcal{E}_{D_t}^{x_1}$ and $\mathcal{E}_{D_t}^{x_2}$ given in (18) and (19), respectively. The proof is thus complete.

On the other hand, as explained in the Remark 1, the SINR for detecting the final message (x_L) at the Lth user given in (28) is different to (10), (11), ..., and (12). Thus, its CDF and EC are also different to them in (27) and (20), respectively. In particular, the CDF of $\lambda_{D_L}^{x_L}$, $F_{\lambda_{D_L}^{x_L}}(y)$ is formulated as

$$F_{\lambda_{D_L}^{x_L}}(y) = \Pr\left\{\lambda_{D_L}^{x_L} < y\right\} = \Pr\left\{\frac{\mathcal{A}_L^2\rho_L P_S}{\sigma_L^2} < y\right\}. \quad (66)$$

It is clear that (66) is different to (26). Therefore, $F_{\lambda_{D_L}^{x_L}}(y)$ is also different to (27), i.e.,

$$F_{\lambda_{D_L}^{x_L}}(y) = \Pr\left\{\mathcal{A}_L^2 < \frac{\sigma_L^2 y}{\rho_L P_S}\right\} = F_{\mathcal{A}_L}\left(\sqrt{\frac{y}{\bar{\lambda}_{D_L}\rho_L}}\right)$$
$$= 1 - \frac{1}{\Gamma(\Lambda_L)}\Gamma\left(\Lambda_L, \Delta_L\sqrt{\frac{y}{\bar{\lambda}_{D_L}\rho_L}}\right). \quad (67)$$

Now, $\mathcal{E}_{D_L}^{x_L}$ is formulated as

$$\mathcal{E}_{D_L}^{x_L} = \frac{1}{\Gamma(\Lambda_L)\ln 2}\int_0^{\infty}\frac{1}{1+y}\Gamma\left(\Lambda_L, \Delta_L\sqrt{\frac{y}{\bar{\lambda}_{D_L}\rho_L}}\right)dy. \quad (68)$$

Based on [50, Eq. (8.4.2.5)] and [50, Eq. (8.4.16.2)], we have

$$(1+y)^{-1} = G_{1,1}^{1,1}\left(y\Big|_0^0\right), \quad (69)$$

$$\Gamma\left(\Lambda_L, \Delta_L\sqrt{\frac{y}{\bar{\lambda}_{D_L}\rho_L}}\right) = G_{1,2}^{2,0}\left(\Delta_L\sqrt{\frac{y}{\bar{\lambda}_{D_L}\rho_L}}\Big|_{\Lambda_L,0}^1\right). \quad (70)$$

Consequently, we have

$$\mathcal{E}_{D_L}^{x_L} = \frac{1}{\Gamma(\Lambda_L)\ln 2}$$
$$\times \int_0^{\infty} G_{1,1}^{1,1}\left(y\Big|_0^0\right)G_{1,2}^{2,0}\left(\Delta_L\sqrt{\frac{y}{\bar{\lambda}_{D_L}\rho_L}}\Big|_{\Lambda_L,0}^1\right)dy.$$
(71)

After applying [50, Eq. (2.24.1.1)], (71) becomes (29) in the Remark 1. The proof is fully complete.

REFERENCES

[1] A. Souzani, M. A. Pourmina, P. Azmi, and M. Naser-Moghadasi, "Physical layer security enhancement via IRS based on PD-NOMA and cooperative jamming," *IEEE Access*, vol. 11, pp. 65956–65967, 2023.

[2] B. Zhuo, J. Gu, W. Duan, G. Zhang, M. Wen, and F. Gao, "RIS-IoE for data-driven networks: New mentalities, trends and preliminary solutions," *IEEE Internet Things Mag.*, vol. 6, no. 2, pp. 102–107, Jun. 2023.

[3] A. Bansal, K. Singh, and C.-P. Li, "Analysis of hierarchical rate splitting for intelligent reflecting surfaces-aided downlink multiuser MISO communications," *IEEE Open J. Commun. Soc.*, vol. 2, pp. 785–798, 2021.

[4] T. N. Nguyen, N. N. Thang, B. C. Nguyen, T. M. Hoang, and P. T. Tran, "Intelligent-reflecting-surface-aided bidirectional full-duplex communication system with imperfect self-interference cancellation and hardware impairments," *IEEE Syst. J.*, vol. 17, no. 1, pp. 1352–1362, Mar. 2023.

[5] A. A. Boulogeorgos and A. Alexiou, "Performance analysis of reconfigurable intelligent surface-assisted wireless systems and comparison with relaying," *IEEE Access*, vol. 8, pp. 94463–94483, 2020.

[6] E. Björnson, Ö. Özdogan, and E. G. Larsson, "Intelligent reflecting surface versus decode-and-forward: How large surfaces are needed to beat relaying?" *IEEE Wireless Commun. Lett.*, vol. 9, no. 2, pp. 244–248, Feb. 2020.

[7] T. N. Do, G. Kaddoum, T. L. Nguyen, D. B. da Costa, and Z. J. Haas, "Multi-RIS-aided wireless systems: Statistical characterization and performance analysis," *IEEE Trans. Commun.*, vol. 69, no. 12, pp. 8641–8658, Dec. 2021.

[8] E. Björnson and L. Sanguinetti, "Power scaling laws and near-field behaviors of massive MIMO and intelligent reflecting surfaces," *IEEE Open J. Commun. Soc.*, vol. 1, pp. 1306–1324, 2020.

[9] K. K. Nguyen, A. Masaracchia, V. Sharma, H. V. Poor, and T. Q. Duong, "RIS-assisted UAV communications for IoT with wireless power transfer using deep reinforcement learning," *IEEE J. Sel. Topics Signal Process.*, vol. 16, no. 5, pp. 1086–1096, Aug. 2022.

[10] D. T. Tam, B. C. Nguyen, L. V. Nguyen, and N. V. Vinh, "Outage and throughput performance of hybrid RISs-relay-aided-wireless systems with imperfect transceiver hardware," *AEU Int. J. Electron. Commun.*, vol. 157, Dec. 2022, Art. no. 154425.

[11] A. Mahmoud, S. Muhaidat, P. C. Sofotasios, I. Abualhaol, O. A. Dobre, and H. Yanikomeroglu, "Intelligent reflecting surfaces assisted UAV communications for IoT networks: Performance analysis," *IEEE Trans. Green Commun. Netw.*, vol. 5, no. 3, pp. 1029–1040, Sep. 2021.

[12] P. Mursia, F. Devoti, V. Sciancalepore, and X. Costa-Pérez, "RISe of flight: RIS-empowered UAV communications for robust and reliable air-to-ground networks," *IEEE Open J. Commun. Soc.*, vol. 2, pp. 1616–1629, 2021.

[13] Y. Li, C. Yin, T. Do-Duy, A. Masaracchia, and T. Q. Duong, "Aerial reconfigurable intelligent surface-enabled URLLC UAV systems," *IEEE Access*, vol. 9, pp. 140248–140257, 2021.

[14] B. K. S. Lima, A. S. De Sena, R. Dinis, D. B. Da Costa, M. Beko, R. Oliveira, and M. Debbah, "Aerial intelligent reflecting surfaces in MIMO-NOMA networks: Fundamentals, potential achievements, and challenges," *IEEE Open J. Commun. Soc.*, vol. 3, pp. 1007–1024, 2022.

[15] E. M. Mohamed, M. Alnakhli, S. Hashima, and M. Abdel-Nasser, "Distribution of multi mmWave UAV mounted RIS using budget constraint multi-player MAB," *Electronics*, vol. 12, no. 1, p. 12, Dec. 2022.

[16] M. Elhattab, M. A. Arfaoui, C. Assi, and A. Ghrayeb, "Reconfigurable intelligent surface enabled full-duplex/half-duplex cooperative non-orthogonal multiple access," *IEEE Trans. Wireless Commun.*, vol. 21, no. 5, pp. 3349–3364, May 2022.

[17] Y. Cheng, K. H. Li, Y. Liu, K. C. Teh, and H. Vincent Poor, "Downlink and uplink intelligent reflecting surface aided networks: NOMA and OMA," *IEEE Trans. Wireless Commun.*, vol. 20, no. 6, pp. 3988–4000, Jun. 2021.

[18] B. C. Nguyen, T. M. Hoang, L. T. Dung, T. Kim, and N. V. Vinh, "On performance of full-duplex UAV system with multiple NOMA users and millimeter-wave communications," *Phys. Commun.*, vol. 55, Dec. 2022, Art. no. 101895.

[19] G. Alnwaimi and H. Boujemaa, "Non orthogonal multiple access using reconfigurable intelligent surfaces," *Wireless Pers. Commun.*, vol. 121, no. 3, pp. 1607–1625, Dec. 2021.

[20] D. Tyrovolas, S. A. Tegos, P. D. Diamantoulakis, and G. K. Karagiannidis, "Synergetic UAV-RIS communication with highly directional transmission," *IEEE Wireless Commun. Lett.*, vol. 11, no. 3, pp. 583–587, Mar. 2022.

[21] Y. Cheng, K. H. Li, Y. Liu, K. C. Teh, and G. K. Karagiannidis, "Non-orthogonal multiple access (NOMA) with multiple intelligent reflecting surfaces," *IEEE Trans. Wireless Commun.*, vol. 20, no. 11, pp. 7184–7195, Nov. 2021.

[22] Z. Q. Al-Abbasi, L. Farhan, and R. S. Alhumaima, "Multiple-intelligent reflective surfaces (Multi-IRSs)-based NOMA system," *Electronics*, vol. 11, no. 23, p. 4045, Dec. 2022.

[23] B. Tahir, S. Schwarz, and M. Rupp, "Analysis of uplink IRS-assisted NOMA under Nakagami-*m* fading via moments matching," *IEEE Wireless Commun. Lett.*, vol. 10, no. 3, pp. 624–628, Mar. 2021.

[24] Y. Xiu, J. Zhao, W. Sun, M. D. Renzo, G. Gui, Z. Zhang, and N. Wei, "Reconfigurable intelligent surfaces aided mmWave NOMA: Joint power allocation, phase shifts, and hybrid beamforming optimization," *IEEE Trans. Wireless Commun.*, vol. 20, no. 12, pp. 8393–8409, Dec. 2021.

[25] T. N. Do, G. Kaddoum, T. L. Nguyen, D. B. da Costa, and Z. J. Haas, "Aerial reconfigurable intelligent surface-aided wireless communication systems," in *Proc. 32nd IEEE Annu. Int. Symp. Pers., Indoor Mobile Radio Commun. (PIMRC)*, Helsinki, Finland, Sep. 2021, pp. 525–530.

[26] K. Zhao, H. Mei, S. Lyu, and L. Peng, "Joint optimization of multiple UAV-mounted RISs deployment and RIS elements allocation," in *Proc. 13th Int. Conf. Inf. Commun. Technol. Converg. (ICTC)*, Jeju Island, South Korea, Oct. 2022, pp. 1193–1197.

[27] S. Solanki, J. Park, and I. Lee, "On the performance of IRS-aided UAV networks with NOMA," *IEEE Trans. Veh. Technol.*, vol. 71, no. 8, pp. 9038–9043, Aug. 2022.

[28] L. Bariah, F. Boukhalfa, W. Jaafar, S. Muhaidat, and H. Yanikomeroglu, "On the performance of RIS-enabled NOMA for aerial networks," in *Proc. IEEE Wireless Commun. Netw. Conf. (WCNC)*, Glasgow, U.K., Mar. 2023, pp. 1–6.

[29] S. K. Singh, K. Agrawal, K. Singh, C.-P. Li, and Z. Ding, "NOMA enhanced hybrid RIS-UAV-assisted full-duplex communication system with imperfect SIC and CSI," *IEEE Trans. Commun.*, vol. 70, no. 11, pp. 7609–7627, Nov. 2022.

[30] Z. Ding, Z. Yang, P. Fan, and H. V. Poor, "On the performance of non-orthogonal multiple access in 5G systems with randomly deployed users," *IEEE Signal Process. Lett.*, vol. 21, no. 12, pp. 1501–1505, Dec. 2014.

[31] L. Yang, Y. Yang, D. B. D. Costa, and I. Trigui, "Outage probability and capacity scaling law of multiple RIS-aided networks," *IEEE Wireless Commun. Lett.*, vol. 10, no. 2, pp. 256–260, Feb. 2021.

[32] P. T. Tran, B. C. Nguyen, T. M. Hoang, X. H. Le, and V. D. Nguyen, "Exploiting multiple RISs and direct link for performance enhancement of wireless systems with hardware impairments," *IEEE Trans. Commun.*, vol. 70, no. 8, pp. 5599–5611, Aug. 2022.

[33] Z. Wang, L. Liu, and S. Cui, "Channel estimation for intelligent reflecting surface assisted multiuser communications: Framework, algorithms, and analysis," *IEEE Trans. Wireless Commun.*, vol. 19, no. 10, pp. 6607–6620, Oct. 2020.

[34] X. Wei, D. Shen, and L. Dai, "Channel estimation for RIS assisted wireless communications—Part I: Fundamentals, solutions, and future opportunities," *IEEE Commun. Lett.*, vol. 25, no. 5, pp. 1398–1402, May 2021.

[35] S. Atapattu, R. Fan, P. Dharmawansa, G. Wang, J. Evans, and T. A. Tsiftsis, "Reconfigurable intelligent surface assisted two–way communications: Performance analysis and optimization," *IEEE Trans. Commun.*, vol. 68, no. 10, pp. 6552–6567, Oct. 2020.

[36] E. Basar, M. Di Renzo, J. De Rosny, M. Debbah, M.-S. Alouini, and R. Zhang, "Wireless communications through reconfigurable intelligent surfaces," *IEEE Access*, vol. 7, pp. 116753–116773, 2019.

[37] Q. Wu and R. Zhang, "Beamforming optimization for wireless network aided by intelligent reflecting surface with discrete phase shifts," *IEEE Trans. Commun.*, vol. 68, no. 3, pp. 1838–1851, Mar. 2020.

[38] A. Hemanth, K. Umamaheswari, A. C. Pogaku, D.-T. Do, and B. M. Lee, "Outage performance analysis of reconfigurable intelligent surfaces-aided NOMA under presence of hardware impairment," *IEEE Access*, vol. 8, pp. 212156–212165, 2020.

[39] P. T. Tran, B. C. Nguyen, T. M. Hoang, and T. N. Nguyen, "On performance of low-power wide-area networks with the combining of reconfigurable intelligent surfaces and relay," *IEEE Trans. Mob. Comput.*, vol. 22, no. 10, pp. 6086–6096, Oct. 2023.

[40] E. M. Mohamed, "Deployment of mmWave multi-UAV mounted RISs using budget constraint Thompson sampling with collision avoidance," *ICT Exp.*, early access, pp. 1–8, Aug. 2023.

[41] Y. Lin, S. Jin, M. Matthaiou, and X. You, "Channel estimation and user localization for IRS-assisted MIMO-OFDM systems," *IEEE Trans. Wireless Commun.*, vol. 21, no. 4, pp. 2320–2335, Apr. 2022.

[42] L. Yang, X. Li, S. Jin, M. Matthaiou, and F.-C. Zheng, "Fine-grained analysis of reconfigurable intelligent surface-assisted mmWave networks," *IEEE Trans. Commun.*, vol. 70, no. 9, pp. 6277–6294, Sep. 2022.

[43] I. Yildirim, A. Uyrus, and E. Basar, "Modeling and analysis of reconfigurable intelligent surfaces for indoor and outdoor applications in future wireless networks," *IEEE Trans. Commun.*, vol. 69, no. 2, pp. 1290–1301, Feb. 2021.

[44] A. Yilmaz and O. Kucur, "Performance of transmit antenna selection and maximal-ratio combining in dual hop amplify-and-forward relay network over Nakagami-*m* fading channels," *Wireless Pers. Commun.*, vol. 67, no. 3, pp. 485–503, Dec. 2012.

[45] W. Han, J. Ge, and J. Men, "Performance analysis for NOMA energy harvesting relaying networks with transmit antenna selection and maximal-ratio combining over Nakagami-*m* fading," *IET Commun.*, vol. 10, no. 18, pp. 2687–2693, Dec. 2016.

[46] A. Jeffrey and D. Zwillinger, *Table of Integrals, Series, and Products*. New York, NY, USA: Academic Press, 2007.

[47] D. T. Tam, N. V. Vinh, and B. C. Nguyen, "Improving the performance of multi-IRS aided millimeter-wave communication systems by transmit antenna selection," *Phys. Commun.*, vol. 56, Feb. 2023, Art. no. 101957.

[48] D. B. D. Costa, H. Ding, and J. Ge, "Interference-limited relaying transmissions in dual-hop cooperative networks over Nakagami-*m* fading," *IEEE Commun. Lett.*, vol. 15, no. 5, pp. 503–505, May 2011.

[49] M. Abramowitz and I. A. Stegun, *Handbook of Mathematical Functions With Formulas, Graphs, and Mathematical Tables*, vol. 9. New York, NY, USA: Dover, 1972.

[50] A. P. Prudnikov, *Integrals and Series* (More special functions), vol. 3, A. P. Prudnikov, Y. A. Brychkov, O. I. Marichev, and G. G. Gould, Eds. Philadelphia, PA, USA: Gordon and Breach, 1998.

LE SI PHU received the B.Sc. degree from Nha Trang University, Nha Trang, Vietnam, in 2008, and the M.B.A. degree from the Open University of Malaysia, in 2013. He is currently pursuing the Ph.D. degree in telecommunication from the VSB—Technical University of Ostrava, Czech Republic, in 2023. He was a Lecturer with the IT Department, Van Lang University, from 2009 to 2020. He is the Managing Director of ACEXIS JSC. His current research interests include electronic design, digital signal processing, MIMO, and intelligent reflecting surfaces.

TAN N. NGUYEN (Member, IEEE) received the B.S. degree in electronics from the Ho Chi Minh University of Natural Sciences, in 2008, the M.S. degree in telecommunications engineering from Vietnam National University, in 2012, and the Ph.D. degree in communications technologies from the Faculty of Electrical Engineering and Computer Science, VSB—Technical University of Ostrava, Czech Republic, in 2019. He joined the Faculty of Electrical and Electronics Engineering, Ton Duc Thang University, Vietnam, in 2013, and since then has been lecturing. His current research interests include cooperative communications, cognitive radio, signal processing, satellite communication, UAV, and physical layer security. He was the Editor-in-Chief of *Advances in Electrical and Electronic Engineering* journal, in 2023.

MIROSLAV VOZNAK (Senior Member, IEEE) received the Ph.D. degree in telecommunications from the Faculty of Electrical Engineering and Computer Science, VSB—Technical University of Ostrava, in 2002, and the Habilitation degree, in 2009. He was a full professor of electronics and communications technologies, in 2017. He has participated in six projects funded by the EU in programs managed directly by the European Commission. Currently, he is the Principal Investigator in the research project QUANTUM5 funded by NATO, which focuses on the application of quantum cryptography in 5G campus networks. He has authored and coauthored more than 100 articles indexed in SCI/SCIE journals. His current research interests include ICT, especially on quality of service and experience, network security, wireless networks, and big data analytics. According to a Stanford University study released in 2020, he is one of the World's Top 2% of Scientists in networking and telecommunications and information and communications technologies. He served as the General Chair for the 11th IFIP Wireless and Mobile Networking Conference, in 2018, and the 24th IEEE/ACM International Symposium on Distributed Simulation and Real-Time Applications, in 2020.

BA CAO NGUYEN received the B.S. degree in electrical engineering from Telecommunication University, Nha Trang, Khanh Hoa, Vietnam, in 2006, the M.S. degree in electrical engineering from the Posts and Telecommunications Institute of Technology, Ho Chi Minh City, Vietnam, in 2011, and the Ph.D. degree in electrical engineering from Le Quy Don Technical University, Hanoi, Vietnam in 2020.

He is currently a Lecturer with Telecommunications University. His current research interests include energy harvesting, full-duplex, spatial modulation, nonorthogonal multiple access, multiple-input multiple-output, reconfigurable intelligent surface, and cooperative communication.

TRAN MANH HOANG received the B.S. degree in communication command from Telecommunications University, Ministry of Defense, Nha Trang, Vietnam, in 2002, the B.Eng. degree in electrical engineering from Le Quy Don Technical University, Hanoi, Vietnam, in 2006, the M.Eng. degree in electronics engineering from the Posts and Telecommunications Institute of Technology, Ho Chi Minh City, Vietnam, in 2013, and the Ph.D. degree in electronics engineering from Le Quy Don Technical University, in 2018.

He has been a Visiting Professor with the School of Information and Communication Engineering, Chungbuk National University, Cheongju, South Korea, since November 2021. He is currently a Lecturer with Telecommunications University, Khanh Hoa, Vietnam. He has authored or coauthored more than 80 papers in refereed international journals and conferences. His current research interests include energy harvesting, UAV, short-packet communication, nonorthogonal multiple access, MIMO, RIS, and signal processing for wireless cooperative communications. He was a recipient of the 2022 IEEE ATC Best Paper Award.

BUI VU MINH received the degree in electrical and electronic engineering from Nguyen Tat Thanh University, Ho Chi Minh City, Vietnam, in 2015, and the master's degree in electrical engineering from the Ho Chi Minh City University of Technology and Education, Ho Chi Minh City, in 2019. In 2014, he joined the Faculty of Mechanical, Electrical, Electronic and Automotive Engineering, Nguyen Tat Thanh University, and the Laboratory-Practice Management, where he was a Lecturer, until 2017. His current research interests include artificial neural networks and wireless networks.

PHUONG T. TRAN (Senior Member, IEEE) was born in Ho Chi Minh City, Vietnam, in 1979. He received the B.Eng. and M.Eng. degrees in electrical engineering from the Ho Chi Minh University of Technology, Ho Chi Minh City, in 2002 and 2005, respectively, and the M.S. degree in mathematics and the Ph.D. degree in electrical and computer engineering from Purdue University, USA, in 2013. In 2007, he was a Vietnam Education Foundation Fellow with Purdue University. In 2013, he joined the Faculty of Electrical and Electronics Engineering, Ton Duc Thang University, Vietnam, and has been the Vice Dean of the Faculty of Electrical and Electronics Engineering, since October 2014. His current research interests include wireless communications and network information theory.

• • •